nature communications

Article

https://doi.org/10.1038/s41467-024-53289-z

Harnessing air-water interface to generate interfacial ROS for ultrafast environmental remediation

Received: 6 June 2024

Accepted: 8 October 2024

Published online: 14 October 2024

Check for updates

Ruijie Xie[1], Kaiheng Guo[1], Yong Li[2], Yingguang Zhang[3], Huanran Zhong[1], Dennis Y. C. Leung[3] & Haibao Huang[1,4]

The air-water interface of microbubbles represents a crucial microenvironment that can dramatically accelerate reactive oxidative species (ROS) reactions. However, the dynamic nature of microbubbles presents challenges in probing ROS behaviors at the air-water interface, limiting a comprehensive understanding of their chemistry and application. Here we develop an approach to investigate the interfacial ROS via coupling microbubbles with a Fenton-like reaction. Amphiphilic single-Co-atom catalyst (Co@SCN) is employed to efficiently transport the oxidant peroxymonosulfate (PMS) from the bulk solution to the microbubble interface. This triggers an accelerated generation of interfacial sulfate radicals ($SO_4^{\bullet-}$), with 20-fold higher concentration (4.48×10^{-11} M) than the bulk $SO_4^{\bullet-}$. Notably, the generated $SO_4^{\bullet-}$ is preferentially situated at the air-water interface due to its lowest free energy and the strong hydrogen bonding interactions with H_3O^+. Moreover, it exhibits the highest oxidation reactivity toward gaseous pollutants like toluene, with a rate constant of 10^{10} M^{-1} s^{-1}-over 100 times greater than bulk reactions. This work demonstrates a promising strategy to harness the air-water interface for accelerating ROS-induced reactions, highlighting the importance of interfacial ROS and its potential application.

The air–water interface, arising from the interplay between air and water molecules, is widely encountered in the fields of atmospheric, biological, prebiotic, and synthetic organic chemistry[1,2]. Recently, our understanding of this microenvironment has evolved dramatically that the chemical reaction rates can be accelerated by many orders of magnitude when occurring at or near the air–water interfaces[3–5]. In particular, the air–water interface can significantly enhance the reactive oxidative species (ROS) reactions compared to that in the bulk phase[6,7]. This remarkable phenomenon particularly gains attention in atmospheric chemistry, where the oxidation kinetics of atmospheric trace gases (e.g., nitric oxide (NO_x) and volatile organic compounds (VOCs)) by ROS are enhanced significantly at the surface of cloud-water droplets[8–10]. These findings from the natural world provide a guide for constructing artificial air–water interfaces to accelerate ROS-induced reactions for practical application, given the pivotal role of ROS in fundamental chemical processes across atmospheric, biological, aquatic, and synthetic organic chemistry domains.

Highly reactive radical species, such as hydroxyl radicals ($HO^{\bullet}$) and sulfate radicals ($SO_4^{\bullet-}$), exhibit remarkable reactivity and possess the capacity to completely oxidize a wide range of organic pollutants into CO_2 and H_2O, rendering them promising for environmental remediation[11–13]. The Fenton and Fenton-like reactions are commonly employed as effective methods to generate ROS[14,15]. These reactions involve the catalytic activation of diverse peroxides, including

[1]School of Environmental Science and Engineering, Sun Yat-sen University, Guangzhou, China. [2]Institute of Applied and Physical Chemistry and Center for Environmental Research and Sustainable Technology, University of Bremen, Bremen, Germany. [3]Department of Mechanical Engineering, The University of Hong Kong, Hong Kong, China. [4]College of Ecology and Environment, School of Chemical Engineering and Technology, Xinjiang University, Urumchi, China. e-mail: seabao8@gmail.com

hydrogen peroxide (H_2O_2) and peroxymonosulfate (PMS), to produce $HO^{\bullet}$ and $SO_4^{\bullet-}$. Despite considerable efforts to further accelerate Fenton or Fenton-like reactions, such as optimizing the catalytic activity with single metal atoms or applying external energy inputs (e.g. UV light, heat), the overall ROS generation rates achieved by these approaches remain limited[16–18]. This is largely due to the inherent kinetic and thermodynamic constraints of the bulk-phase reactions, which restrict the maximum achievable concentrations of the highly ROS[19,20]. In addition, the ROS are quickly consumed by competing side reactions or scavenged by various species present in the solution, limiting their overall effectiveness for environmental remediation[21].

To overcome the bulk-phase limitations, harnessing the air–water interface provided by microbubble represents a promising strategy to dramatically accelerate certain Fenton reactions[22,23]. Notably, previous investigations have underscored the intriguing potential of ROS generated at the air–water interface of microbubbles and suggested that these species may play pivotal roles in environmental remediation applications[24–26]. However, whether interfacial ROS are indeed generated at microbubble surfaces, as well as the chemical behaviors of such species, remain unclear[27]. Two key challenges have hindered progress in this area: Firstly, there is an inherent difficulty in directly probing ROS generation and its associated chemical characteristics at the dynamic, transient microbubble interface within the bulk solution phase. Secondly, transporting the required peroxide oxidants, such as H_2O_2 or PMS, from the bulk phase to the microbubble surface is limited, given that these reactants are initially present predominantly in the solution before microbubble introduction.

Therefore, in this study, we develop a promising strategy to investigate interfacial ROS chemistry and explore its promising application. We employed an amphiphilic single-Co-atom catalyst (Co@SCN) that can stably attach to the microbubble and efficiently shuttle the key oxidant PMS from the bulk solution to the microbubble surface. At the microbubble interface, the Co@SCN catalyst triggered a highly accelerated Fenton-like reaction of Co@SCN-PMS, resulting in the local generation of a markedly higher concentration of $SO_4^{\bullet-}$ - up to 20-fold greater (4.48×10^{-11} M) compared to the bulk solution. Notably, using in-situ epifluorescence experiments and ab initio molecular dynamics simulations, we provided direct evidence that the generated $SO_4^{\bullet-}$ is preferentially situated at the air–water interface rather than in the bulk solution. This interfacial preference is attributed to the lowest free energy of $SO_4^{\bullet-}$ at the air–water interface and the strong hydrogen bonding interactions between $SO_4^{\bullet-}$ and H_3O^+ in this environment. Moreover, the interfacial $SO_4^{\bullet-}$ has the lowest energy barrier and the highest oxidation reactivity toward gaseous pollutants like toluene with a rate constant of 10^{10} M^{-1} s^{-1}, much higher than those in the bulk reactions by more than 2 orders of magnitude. The specific natures of interfacial ROS result in the ultrafast oxidation performance at the interface, providing deeper insight into the fundamental mechanism and engineering application of the air–water interface.

Results and discussion

Morphological and structural characterizations

The synthesis procedures for the amphiphilic Co@CNS nanospheres are illustrated in Fig. 1a, with detailed information provided in Supplementary Method 2. In brief, monodispersed SiO_2 nanospheres with a uniform diameter of about 50 nm (Supplementary Fig. 1) were ultrasonically dispersed in the dopamine hydrochloride (PDA) solution. After stirring for 24 h, PDA was adsorbed on the surface of SiO_2 nanospheres to form the PDA-modified SiO_2 nanospheres (PDA@SiO_2). The PDA@SiO_2 nanospheres were harvested by centrifugation and were washed with deionized water to remove the excess PDA. Then, the PDA@SiO_2 precursors were dispersed homogeneously in the cyanamide solution, and cobalt nitrate solution was added drop by drop to this suspension under ultrasonic conditions. Subsequently, the resulting mixture was stirred for 5 h, and the solid products were collected via centrifugation, washed, and dried in a vacuum oven at 60 °C, yielding Co@cyanamide/PDA/SiO_2 nanospheres. Finally, Co@cyanamide/PDA/SiO_2 nanospheres were calcined at 600 °C for 4 h under an N_2 atmosphere, resulting in the formation of Co@SCN nanospheres.

The scanning electron microscopy (SEM) image (Fig. 1b) reveals the uniform spherical morphology of Co@SCN, with the size distribution ranging from 45 to 65 nm for approximately 81% of the nanospheres (Supplementary Fig. 2). The high-resolution transmission electron microscopy (HRTEM) image (Fig. 1c) clearly depicts a notably rougher surface on the Co@SCN compared to the smooth appearance of bare SiO_2 nanoparticles (Supplementary Fig. 3), indicating the presence of the core-shell structure. Furthermore, the XRD pattern of Co@SCN (Supplementary Fig. 4) exhibits two broad diffraction peaks at 22.0° and 25.7°, attributed to the amorphous SiO_2 and the (002) planes of graphitized carbon, respectively[28]. These observations strongly indicate that the graphitic carbon was successfully encapsulated on the SiO_2 nanoparticle to form the core-shell structure. Additionally, the selected HRTEM images of a Co@SCN nanoparticle (Fig. 1d, Supplementary Fig. 5) clearly display the wrinkle shell assembled by irregularly shaped graphite carbon nanosheets. The corresponding ring-like selected area electron diffraction (SAED) pattern (inset image of Fig. 1d) further confirms the absence of lattice fringe associated with crystalline Co phases, suggesting the existence of Co species in an atomically dispersed form. Notably, although the graphitic carbon shell displayed a thickness of approximately 5 nm (as shown in the HRTEM image, Fig. 1d), the Co species were highly concentrated on this layer, as indicated by the mapping image (Fig.1f). To validate the distribution of isolated Co atoms, the atomic-resolution high-angle annular dark-field scanning transmission electron microscopy (HAADF-STEM) was conducted. As depicted in Fig. 1g, h, abundant bright spots corresponding to Co species were isolated and atomically distributed on the graphitized carbon shell, with no discernible larger particles or crystalline Co phases observed, thereby demonstrating the presence of Co single atoms. Additionally, the Co content on the Co@SCN surface was determined to be 1.0 wt% by X-ray photoelectron spectroscopy (XPS), consistent with the total Co content of Co@SCN (1.2 wt%) measured by inductively coupled plasma optical emission spectrometry (ICP). These findings suggest that most single Co atoms were anchored on the catalytic surface, providing a high exposure of catalytic active sites for Co@SCN.

We subsequently employed the X-ray absorption near-edge structure (XANES) and the extended X-ray absorption fine structure (EXAFS) spectra to confirm the coordination environment of Co atoms. As shown in the XANES spectra (Fig. 2a), the position of the rising edge for Co@SCN closely resembled with that of CoO, indicating that the average valence state of cobalt in Co@SCN was Co^{2+}. The Fourier transform EXAFS (FT-EXAFS) spectra show that the Co element in Co@SCN was mainly coordinated with nitrogen (N) atoms, with a bond length of 1.54 Å corresponding to the Co–N bonding configuration (Fig. 2b)[29]. Meanwhile, no obvious peaks assigned to the Co–Co bond at 2.18 Å were observed, thus further corroborating the formation of a single Co atom. To confirm the local coordination configuration, the quantitative least-squares EXAFS curve-fitting analyses were used to reveal the first shell of the Co atom in Co@SCN. The structural model and detailed fitted parameters are presented in Supplementary Fig. 6 and Supplementary Table 1. The Fourier transforms of the Co K-edge EXAFS spectra of Co@SCN can be well fitted to the Co–N backscattering path with a five-coordination number (Fig. 2c). The wavelet transforms (WT) contour plot of Co@SCN exhibited distinct differences from those of standard samples of Co foil, CoO and Co_3O_4 (Fig. 2d–g). Especially, the WT contour plot of Co@SCN with only one intensity maximum at 1.54 Å was ascribed to Co–N coordination, and there was no Co–Co coordination as well as Co–O coordination observed for Co@SCN, further confirming its

https://doi.org/10.1038/s41467-024-53289-z

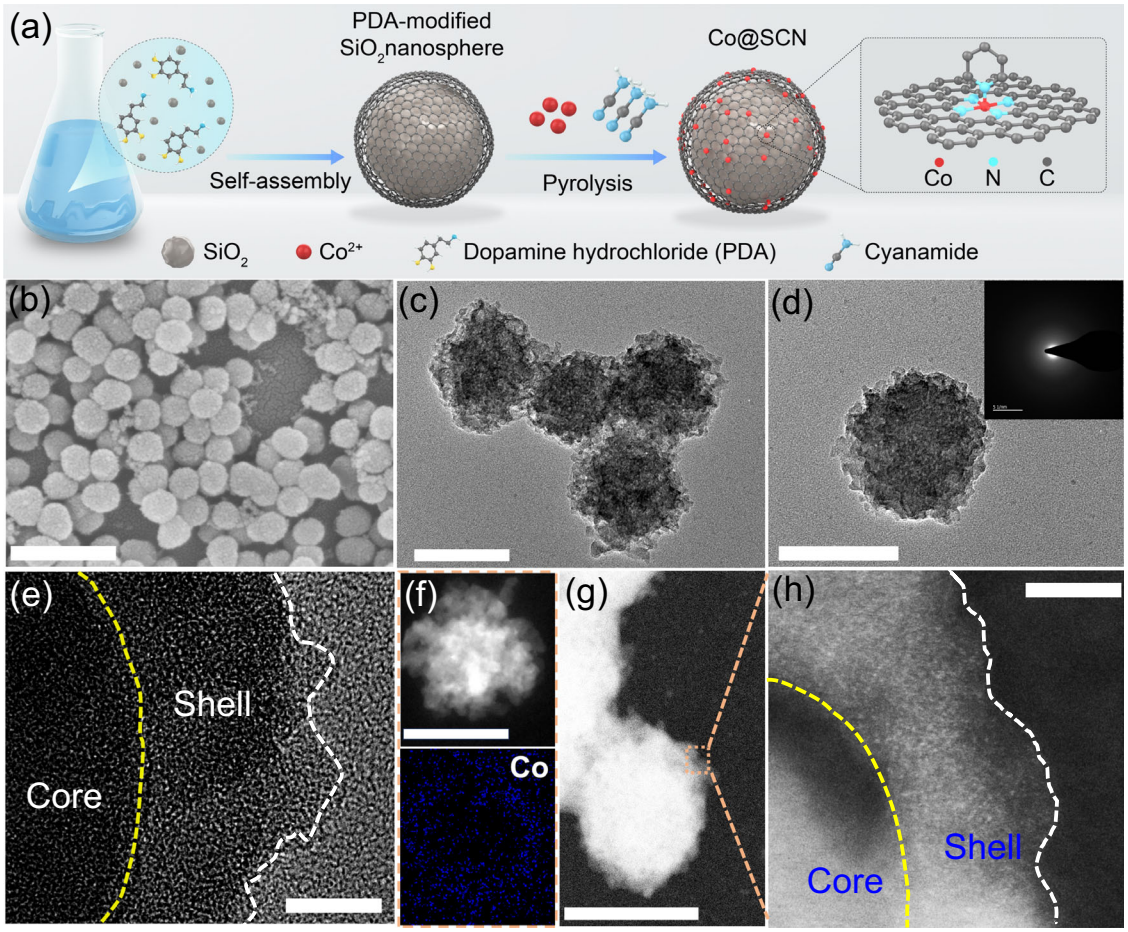

Fig. 1 | Morphological and structural characterizations. a Schematic illustration of the synthesis of Co@SCN; **b** SEM image of Co@SCN; **c**, **d** HRTEM images of Co@SCN, inset: the corresponding ring-like SAED pattern of the image (**d**); **e** Magnified HRTEM image of core-shell structure of Co@SCN; **f** EDS mapping images of Co element in Co@SCN; **g**, **h** HAADF-STEM of Co@SCN. Scale bars: **b** 100 nm; **c**, **d**, **f**, **g** 50 nm; **e**, **h** 2 nm.

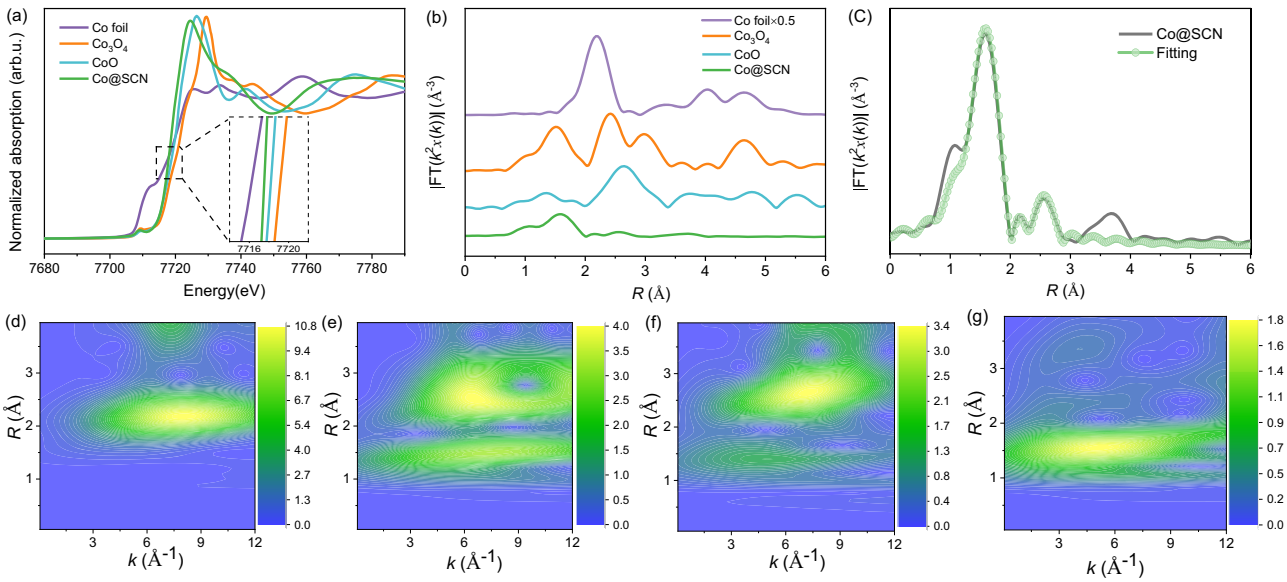

Fig. 2 | Local environment of Co atom in Co@SCN. a, **b** Normalized XANES spectra and k^2-weight FT-EXAFS spectra of Co foil, Co_3O_4, CoO and Co@SCN in *R*-space, inset: the magnified image of Normalized XANES spectra; **c** k^2-weight FT-EXAFS fitting curves of Co@SCN; **d**–**g** WT-EXAFS for the Co element of Co foil, Co_3O_4, CoO and Co@SCN, respectively.

https://doi.org/10.1038/s41467-024-53289-z

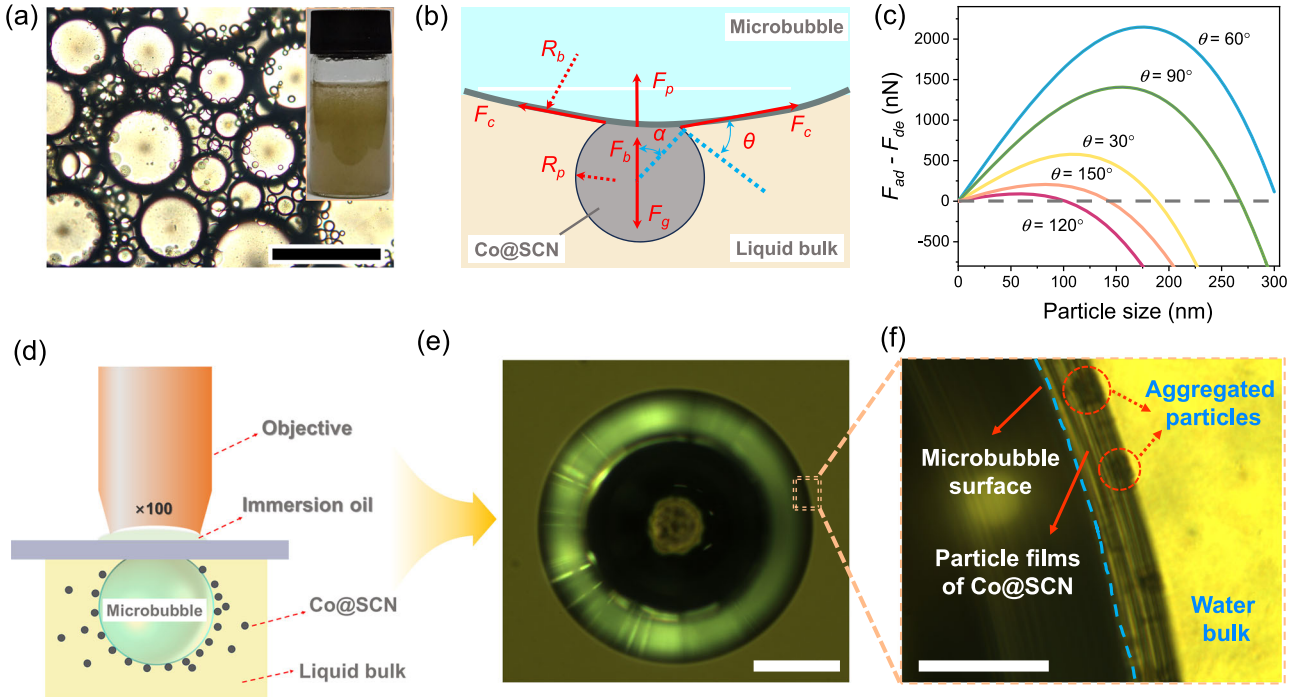

Fig. 3 | Attachment capability of Co@SCN at the aqueous interface. a Formation of the oil-in-water (O/W) Pickering emulsion upon shaking a mixed solution (inset) containing 0.1 wt% Co@SCN, toluene, and water; **b** Schematic illustration of Co@SCN attachment to the microbubble surface and the representation of involving forces at the microbubble surface, here, R_p is the radius of Co@SCN, R_b is the radius of microbubble, F_p is the capillary pressure outside the gas bubble, F_b is the buoyancy force, F_g is the gravitational force, F_c is the surface tension force of the liquid and θ is the contact angle; **c** Relationship of particle sizes and contact angles toward the acting forces of Co@SCN attachment at bubble surface; **d** Schematic illustration of a microbubble directly visualized by reflected-light digital video microscopy; **e**, **f** Microscopy images of a microbubble and the interconnected Co@SCN film at the microbubble surface, respectively; Scale bars: **a** 400 μm, **e** 100 μm, **f** 10 μm.

single-atom feature. All these extensive experimental and simulation results reveal that, in Co@SCN, the single Co atom with CoN_5 coordination configuration has indeed been effectively incorporated into the N-doped graphitic carbon shell.

Attachment capability of Co@SCN at the air–water interface

Upon contact, solid particles can be captured by microbubbles from the aqueous environment to the interfaces, with the attachment capability strongly influenced by its surface property of hydrophilic/hydrophobic groups and the interaction forces involved[30–32]. To assess the surface properties, Co@SCN nanoparticles were dispersed in polar and nonpolar solvents, such as ethanol, water, cyclohexane, and toluene. As illustrated in Supplementary Fig. 7, Co@SCN was well-dispersed in these solvents and thus the mixture was clear and homogeneous, suggesting the amphiphilic property of Co@SCN. Furthermore, when a Co@SCN/toluene/water mixture (inset image of Fig. 3a) was vigorously shaken, it yielded a stable oil-in-water (O/W) Pickering emulsion for more than three months (Fig. 3a). The optical microscopy images of the O/W Pickering emulsion reveal spherical droplets, confirming that Co@SCN nanoparticles can effectively stabilize the oil droplets at the oil-water interface. This observation highlights the inherent amphiphilic surface of Co@SCN. The surface functional group of Co@SCN was further evaluated by Fourier transform infrared (FTIR) spectroscopy (Supplementary Fig. 8). As compared to the SiO_2 nanoparticle, Co@SCN exhibited a significant reduction of the –OH groups (located at 3400 cm^{-1} and 980 cm^{-1}), accompanied by the emergence of new peaks associated with the graphite-like plane (located at 1200-1600 cm^{-1})[33]. It is noteworthy that the SiO_2 core exhibited high hydrophilicity due to the abundance of -OH groups, whereas the N-doped graphitic carbon shell exhibited hydrophobic properties due to its graphite plane with the nonpolar nature of sp^2 carbon[34]. Therefore, this strategic combination balances the hydrophilic and hydrophobic groups on the Co@SCN surface, resulting in the desired amphiphilic properties.

The interaction force between the microbubble and the particle was calculated to further support the attachment capacity of Co@SCN. We commenced with the analysis of forces on a spherical particle attached to a significantly large bubble so that the local bubble–particle geometry and the associated forces could be depicted as shown in Fig. 3b and Supplementary Method 3. The attachment capacity in the particle-bubble system was determined by the interplay of detachment force (F_{de}) and adhesive force (F_{ad}). Particularly, particle gravity governed the former, while the latter was influenced by capillary, pressure, and static buoyancy forces. The integration of F_{ad} and F_{de} resulted in a force function $f\left(R_p, \theta\right) = \pi R_p \sigma(1-\cos\theta) - \frac{4\pi R_p^3 \rho^g}{3}$ that only related to particle size (R_p) and contact angles (θ). We consistently maintained contact angles at 30°, 60°, 90°, 120°, and 150° to systematically assess the impact of particle size on the forces acting on particles-bubble (Fig. 3c). Across all chosen contact angles, the forces increased with larger particles until reaching a plateau. Further increases in particle size led to a decline in force. Notably, our analysis emphasizes the consistent positive forces exhibited by Co@SCN nanoparticles, with a particle size ranging from 40 to 80 nm, for all selected contact angles. This underscores the robust trapping capability of Co@SCN nanoparticles by the microbubble.

Furthermore, the attachment of Co@SCN to the air–water interface was directly visualized using reflected-light digital video microscopy. The air–water interface was formed by bubbling a microbubble in the Co@SCN solution and pressing this microbubble against an optically smooth glass plate, which enabled us to directly visualize the behavior of Co@SCN nanoparticles at the air–water interface (Fig. 3d). A microbubble with the clear interface was observed as presented in Fig. 3e. The magnified microscopy image of microbubble surface (Fig. 3f) and its corresponding video

https://doi.org/10.1038/s41467-024-53289-z

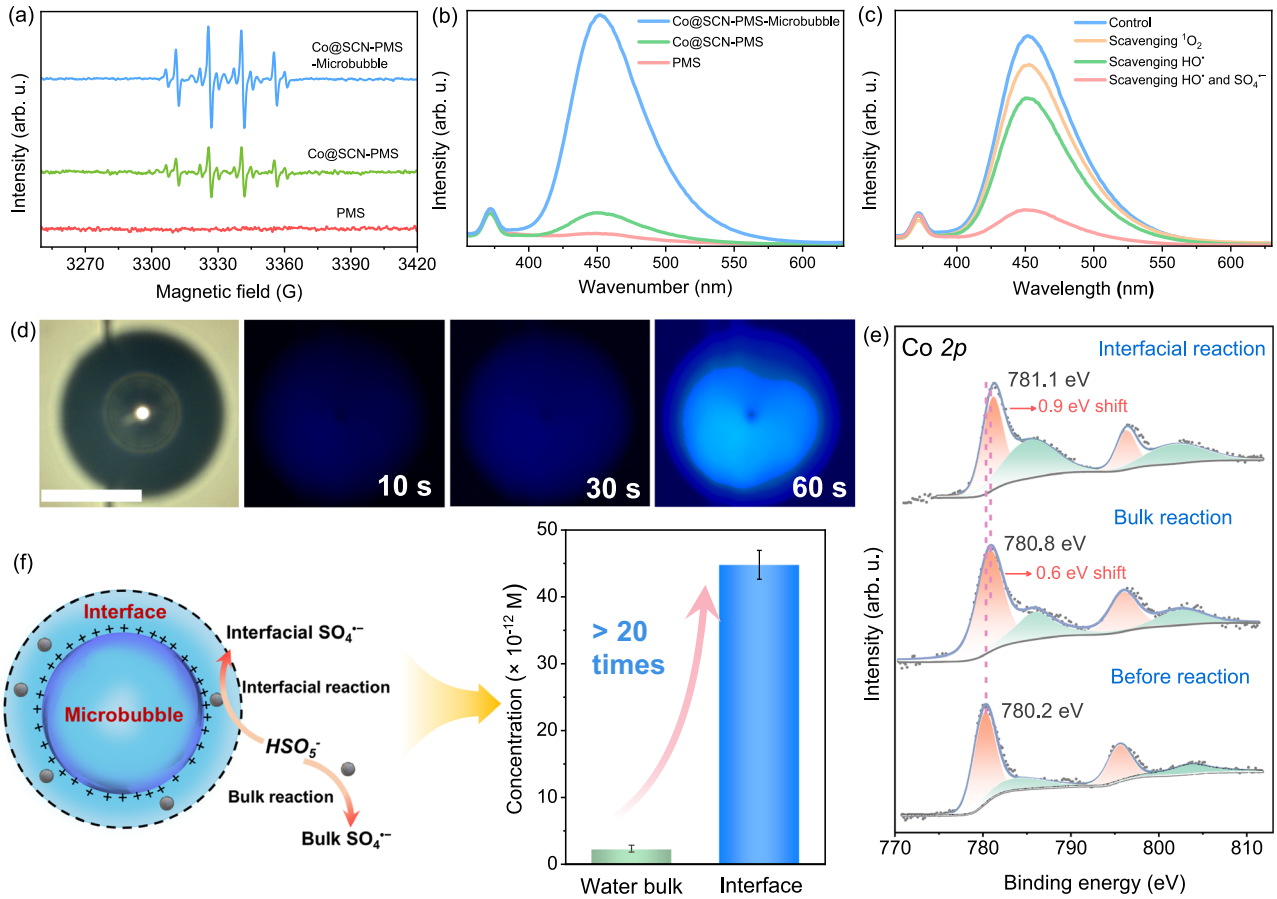

Fig. 4 | Catalytic generation of ROS at the air–water interface. a EPR spectra of the generated ROS in Co@SCN-PMS in the presence/absence of microbubbles; **b** Effect of microbubbles on the 7-hydroxycoumarin production in the Co@SCN-PMS system; **c** Effect of different scavengers on the 7-hydroxycoumarin production in the Co@SCN-PMS-Microbubble system; **d** Brightfield and fluorescence images of a microbubble during different reaction time in the Co@SCN-PMS-Microbubble system; **e** XPS spectrum of Co@SCN before and after interface/bulk reactions for Co *2p*; **f** Schematic illustration of the catalytic generation of $SO_4^{•-}$ at the interface and in the solution bulk, and their respective concentrations (Error bars represent the standard deviation of 2 independent measurements). Conditions: [Co@SCN] = 0.01 g L^{-1}, [PMS] = 0.1 g L^{-1}, [DMPO] = 100 μM, [Coumarin] = 1.0 mM for b = 20 μM for d, [EtOH] = [TBA] = [TEMP] = 10 mM, pH = 5.6. Scale bar for **d**: 300 μm.

(see Supplementary Movie 1) further show that an interconnected Co@SCN film was formed on the microbubble surface, with observable particle motion, confirming the strong attachment of Co@SCN to the air–water interface.

Catalytic generation of ROS at the air–water interface

The catalytic activity of Co@SCN in Fenton-like reactions was assessed in the presence of microbubbles. As a single-Co-atom catalyst, Co@SCN can activate PMS efficiently to produce HO•, $SO_4^{•-}$ and $^1O_2$. Notably, the generation of these ROS increased significantly in the presence of microbubbles, as demonstrated by the ESR measurements (Fig. 4a and Supplementary Fig. 9). When using coumarin as a representative probe for ROS, the specific fluorescence intensity of its oxidative product (7-hydroxycoumarin) was increased dramatically in the presence of microbubbles, further affirming the enhancement of ROS production (Fig. 4b)[35]. Among these ROS, $SO_4^{•-}$ was demonstrated to be the dominant species for coumarin oxidation in the Co@SCN-PMS-Microbubble system by the scavenging experiments (Fig. 4c). The intensity of 7-hydroxycoumarin decreased by approximately 15% in the presence of TBA (a scavenger for HO•), whereas the intensity diminished significantly by 90% in the presence of EtOH (a scavenger for both HO• and $SO_4^{•-}$). The role of $^1O_2$ was further excluded by the insignificant decrease of ROS production in the presence of TEMP (a scavenger for $^1O_2$). Despite the introduction of microbubbles could increase the dissolved O_2 concentration, the dissolved O_2 hardly affected $SO_4^{•-}$ generation in this system, as evidenced by comparable rises in 7-hydroxycoumarin production observed with both air-microbubbles and N_2-microbubbles (Supplementary Fig. 10)[36].

We also investigated the ROS generation when using CoO_x@SiO_2 and CoO_x@C_3N_4 as the hydrophilic catalyst and hydrophobic catalyst, respectively (see Supplementary Fig. 11 and Supplementary Note 1). Unlike the situation with the Co@SCN catalyst, the presence of microbubbles didn't enhance the production of ROS significantly in either the CoO_x@SiO_2-PMS or CoO_x@C_3N_4-PMS systems. Given that the balance between hydrophilic and hydrophobic properties in Co@SCN facilitated its adherence at the air–water interface, we propose that the catalytic reaction of Co@SCN-PMS was accelerated at the microbubble surface, leading to the enhancement of $SO_4^{•-}$ production.

To confirm this hypothesis, we conducted epifluorescence microscopy to visually detect the in-situ $SO_4^{•-}$ generation when microbubbles were present. As depicted in Fig. 4d, when using coumarin as the fluorescent probe for $SO_4^{•-}$, distinct and bright blue fluorescence was observed at the microbubble surface. Subsequently, the fluorescence intensity at the microbubble surface became more significant with increasing reaction time from 10 s to 60 s. In contrast, negligible fluorescence was observed in the Co@SCN-PMS system without microbubbles until 15 min (Supplementary Fig. 12). These observations strongly confirm the acceleration of the Co@SCN-PMS reaction by the microbubble surface, resulting in the enhancement of $SO_4^{•-}$.

Prior research has indicated that the interface of microbubble possesses a strong intrinsic electric field (~10^9 V m^{-1}), which has

https://doi.org/10.1038/s41467-024-53289-z

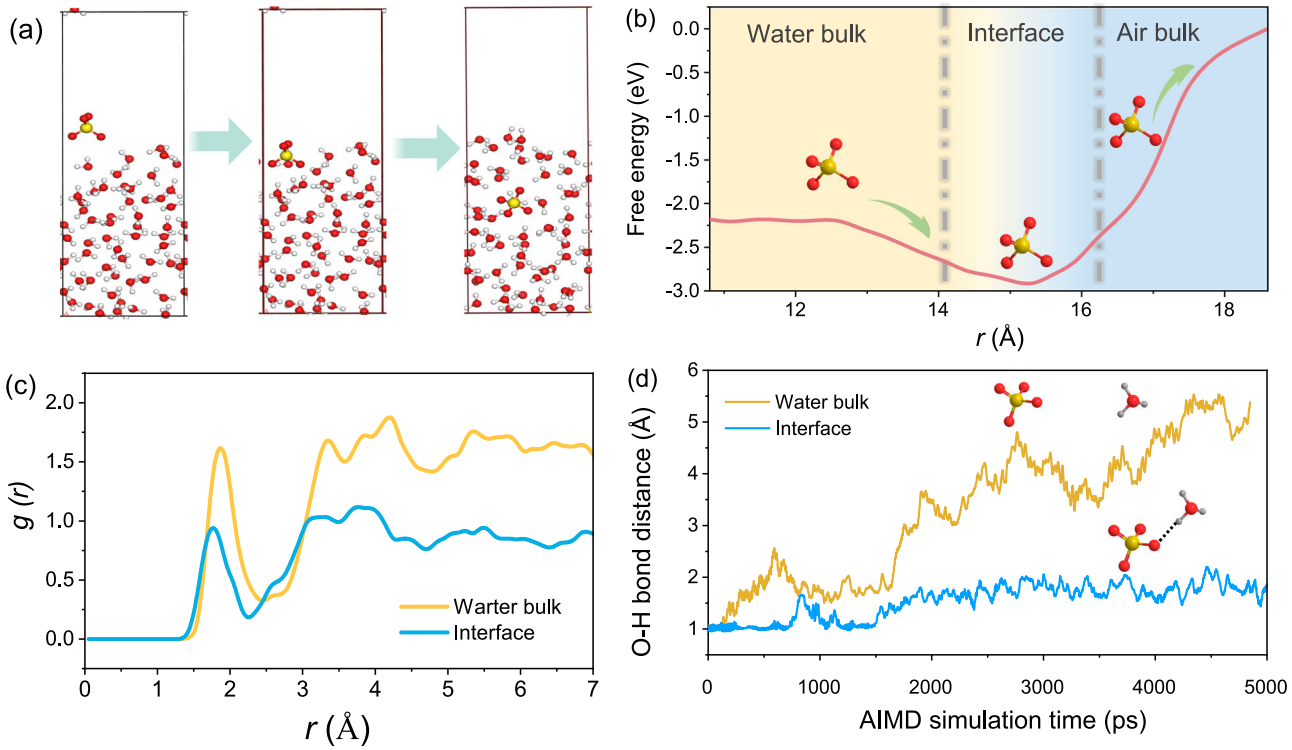

Fig. 5 | Enrichment mechanism of interfacial $SO_4^{\bullet-}$. **a** Snapshots of AIMD simulations illustrating the transition of $SO_4^{\bullet-}$ from the gas phase to the liquid phase at 298 K. **b** Variation in free energy of $SO_4^{\bullet-}$ during its transfer from the gas phase to the liquid phase; **c** Radial distribution function (RDF, *g(r)*) for the H_3O^+-$SO_4^{\bullet-}$ intermediates varying with the distance between $O^{SO4\bullet-}$ and H^{H3O+} in the liquid phase and at the interface; **d** Variation in the distance between $O^{SO4\bullet-}$ and H^{H3O+} in the liquid phase and at the interface, as observed in AIMD simulations.

significant potential to improve electron transfer[37]. As $SO_4^{\bullet-}$ is mainly generated via the activation of PMS through the one-electron redox cycle of the Co atom in the Fenton-like reaction, we supposed that the enhanced $SO_4^{\bullet-}$ production stemmed from the acceleration of electron transfer at the microbubble surface. To confirm this possibility, we employed XPS to determine the electron-transfer capacity of the Co element in Co@SCN in the presence and absence of microbubble. Figure 4e shows that the peak position of the Co element shifted toward a higher energy level by 0.9 eV after its reaction with PMS in the presence of microbubble, while the shift observed after the bulk reaction of Co@SCN-PMS was lower at 0.6 eV. This finding indicates that the presence of Co@SCN on the microbubble surface enhances its electron-transfer capacity compared to the water bulk, resulting in an accelerated catalytic reaction rate. Therefore, it is reasonably concluded that the attachment of the Co@SCN catalyst to the microbubble surface creates a microenvironment that facilitates the acceleration of the Co@SCN-PMS reaction. As shown in Fig. 4f, PMS molecules were adsorbed by Co@SCN from the solution bulk to the microbubble surface, followed by the activation to generate $SO_4^{\bullet-}$. This process was significantly accelerated due to the microbubble surface's ability to expedite the one-electron-transfer pathway. As a result, the concentration of $SO_4^{\bullet-}$ in the Co@SCN-PMS-Microbubble system was significantly enhanced to 4.48×10^{-11} M, substantially higher than those in the bulk (2.33×10^{-12} M) and most reported Fenton-like systems (10^{-15}-10^{-12} M, see Supplementary Note 2 and Supplementary Table 2).

Enrichment mechanism of interfacial $SO_4^{\bullet-}$

As $SO_4^{\bullet-}$ mainly exists in the solution bulk, the significant enhanced interfacial $SO_4^{\bullet-}$ raises two crucial questions: (1) why $SO_4^{\bullet-}$ preferentially accumulates at the microbubble interface rather than transport to the bulk phase, and (2) what the underlying driving force behind this phenomenon is? To explore the first question, classical ab initio molecular dynamics (AIMD) simulations were conducted. Firstly, we examined the free energy variation of $SO_4^{\bullet-}$ upon its transfer from the gas phase to the liquid phase, a parameter that has not been previously reported for $SO_4^{\bullet-}$. As illustrated in Fig. 5a, b, when $SO_4^{\bullet-}$ moved from the gas phase toward the liquid phase, the free energy decreased from 0 to −0.52 kcal mol^{-1} and then increased to a plateau of −0.35 kcal mol^{-1}. The minimum free energy was observed at the air–water interface ($z = 15.3$ Å), signifying that the thermodynamically most stable configuration for $SO_4^{\bullet-}$ occurs at this position. This noteworthy result provides a theoretical underpinning for the experimental findings that $SO_4^{\bullet-}$ is preferentially situated at the microbubble interface, contributing to the enrichment of $SO_4^{\bullet-}$.

Furthermore, our AIMD simulations unveil that $SO_4^{\bullet-}$ within the liquid phase significantly perturbed the structural arrangement of water molecules in the first and second solvation shells. Interestingly, at the air–water interface, this perturbation effect was conspicuously absent, indicating the presence of an underlying "compelling force" behind the observed behavior at the air–water interface. The hydronium ions (H_3O^+) were primarily hypothesized to stabilize $SO_4^{\bullet-}$ through strong hydrogen bonding interactions, as they are the main ions that accumulate at the air–water interface under acidic conditions[38]. To substantiate this hypothesis, we further explored the interaction between $SO_4^{\bullet-}$ and H_3O^+ by investigating the structural features of $SO_4^{\bullet-}$ at the air–water interface and in the bulk phase by employing the radial distribution functions (Fig. 5c). For $SO_4^{\bullet-}$ within the bulk phase, the initial peak of the $O^{SO4\bullet-}$-H^{H3O+} bond distance was observed at $r = 1.9$ Å, indicating the presence of the hydrogen bonding between $O^{SO4\bullet-}$ and H^{H3O+}. Interestingly, this hydrogen bonding was found to be more compacted at the air–water interface, with a reduced bond distance of $r = 1.7$ Å, suggesting a stronger hydrogen bonding interaction between H_3O^+ and $SO_4^{\bullet-}$ at the air–water interface. Furthermore, the hydrogen bonding interaction was stable at the air–water interface, as evidenced by the consistently ~1.7 Å bond distance of $O^{SO4\bullet-}$-H_3O^+ throughout the entire AIMD simulation (Fig. 5d).

https://doi.org/10.1038/s41467-024-53289-z

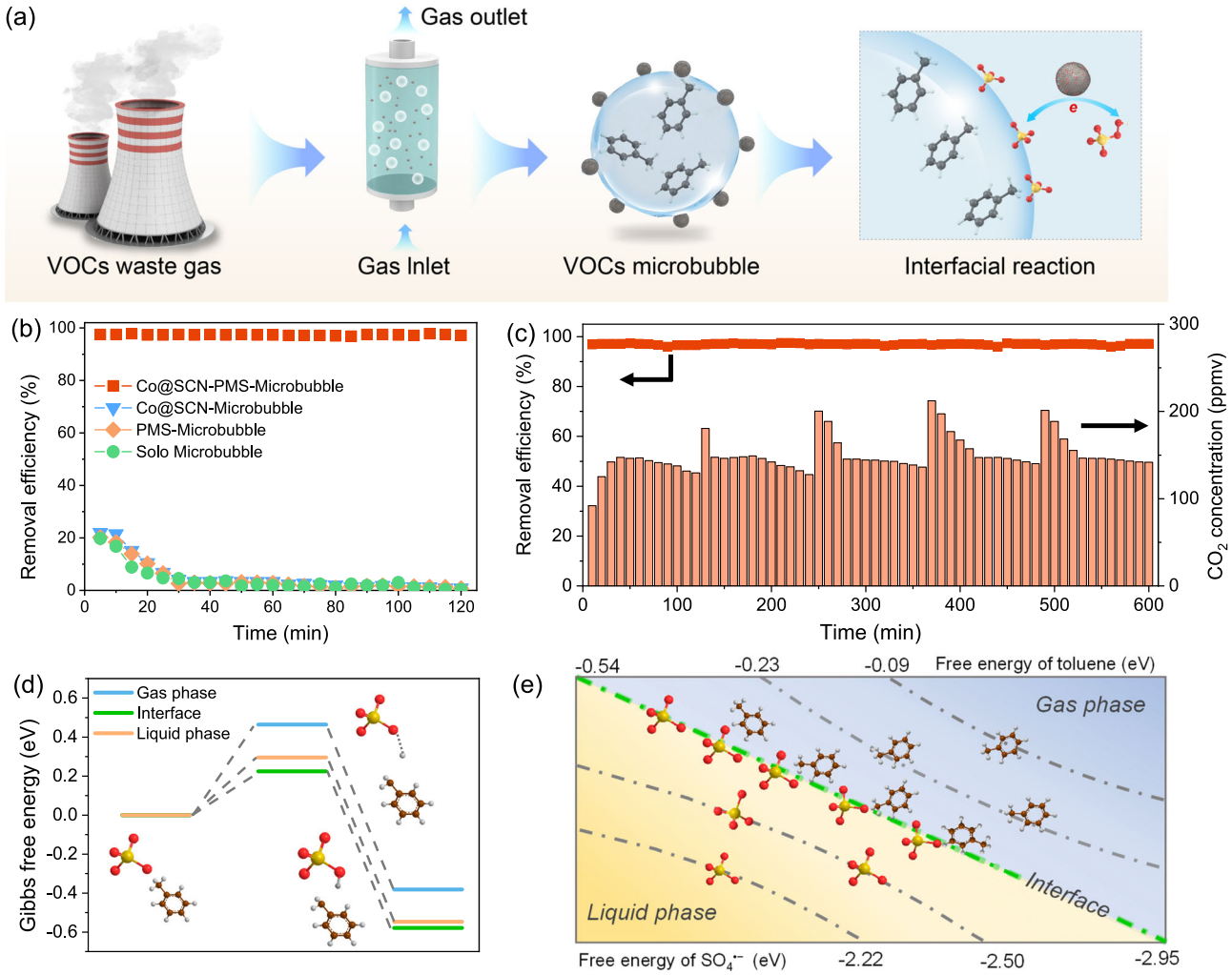

Fig. 6 | Oxidation performance of interfacial $SO_4^{\bullet-}$. **a** Schematic illustration of the Co@SCN-PMS-Microbubble system for the purification of VOCs waste gas; **b** Control experiments of toluene oxidation under different microbubble conditions; **c** Long-term performance of toluene oxidation via multiple additions of PMS in the Co@SCN-PMS-Microbubble system; **d** Calculated potential energy diagrams for toluene oxidation to two key reaction intermediates by $SO_4^{\bullet-}$ and Gibbs free energy comparison of corresponding reactions in gas phase, interface and liquid phase; **e** Comparison of the free energy changes of $SO_4^{\bullet-}$ and toluene in the gas-to-liquid phase transition. Conditions of **b** and **c**: [Co@SCN] = 0.2 g L^{-1}, [PMS] = 2.0 g L^{-1} for each 120 min reaction, pH = 3.0, $[Toluene]_{inlet}$ = 30 ppmv.

In contrast, this distance rapidly increased to over 4.5 Å in the liquid phase, indicative of an unstable interaction. These outcomes unequivocally demonstrate that the stable confinement of $SO_4^{\bullet-}$ at the air–water interface was primarily attributed to the robust hydrogen bonding with H_3O^+.

Ultrafast oxidation capability of interfacial $SO_4^{\bullet-}$

It is imperative to explore the oxidation potential of interfacial $SO_4^{\bullet-}$, which received limited attention in previous studies. Herein, we conducted the Co@SCN-PMS-microbubble system (Setup is shown in Fig. 6a) to produce interfacial $SO_4^{\bullet-}$ for the purification of air pollutants. Toluene, chosen as a hydrophobic and hazardous air pollutant in the atmosphere, was filled within the microbubble to ensure optimal contact with interfacial $SO_4^{\bullet-}$. As toluene microbubbles traversed the solution bulk, toluene underwent a two-step removal process: absorption and oxidation. During adsorption, toluene molecules migrate to the microbubble surface driven by concentration gradient. Subsequently, in the oxidation stage, toluene molecules were oxidized by the interfacial $SO_4^{\bullet-}$ at the microbubble surface.

Through analyzing the outlet toluene concentration from the water bulk, it was interesting to find that toluene was removed by over 99% in this system, despite a brief retention time (approximately 7.0 s) of toluene microbubbles within the solution bulk (Fig. 6b). Moreover, this exceptional performance remained stable over a continuous 2-h operation with the introduction of toluene microbubbles. In contrast, sole microbubbles, PMS-microbubble, or Co@SCN-microbubble systems alone exhibited minimal contribution to the purification of toluene. This finding suggests that the high efficiency of toluene purification was attributed to the interfacial $SO_4^{\bullet-}$ oxidation step. To further validate this conclusion, the toluene concentration in the water bulk was directly measured using membrane inlet mass spectrometry (MIMS), a highly sensitive technique for detecting VOCs at low levels (ppb). Remarkably, even with the continuous introduction of toluene microbubbles into the solution over a 2-h period, no detectable toluene was observed within the solution bulk of the Co@SCN-PMS-microbubble system (Supplementary Fig. 13). In contrast, a gradual increase in toluene concentration was observed in the absence of Co@SCN-PMS, indicating the absorption of toluene into the solution. These results confirm that toluene was oxidized by interfacial $SO_4^{\bullet-}$ rather than being absorbed in the solution bulk. The roles of interfacial $SO_4^{\bullet-}$ in toluene degradation in the Co@SCN-PMS-microbubble were further elucidated through radical scavenging tests. As shown in Supplementary Fig. 14, the toluene removal efficiency decreased by 93% in the presence of EtOH, while it decreased by 12% with TBA.

In addition, the toluene removal efficiency only decreased by 5% in the presence of TEMP, further excluding the role of $^1O_2$ on toluene oxidation. These results strongly indicate that interfacial $SO_4^{\bullet-}$ played the predominant role in toluene oxidation.

Furthermore, the oxidation efficiency of toluene in the Co@SCN-PMS-microbubble system was systematically investigated under various conditions. Initially, we examined the influence of solution pH on toluene removal. As illustrated in Supplementary Fig. 15, the removal efficiency was significant at pH 3–6.5, but then decreased to 70% at pH 9 and further dropped to 30% at a basic condition of pH 11. This implies that an acidic solution was more conducive to toluene degradation in the Co@SCN-PMS-microbubble system. It is essential to note that solution pH plays a pivotal role in determining the ζ-potential of the microbubble, which in turn affects the electrostatic attraction of ions at the interface[39]. In our experiments, the ζ-potential of the toluene-microbubble solution decreased markedly from +19.2 mV at pH 3.0 to −45.3 mV at pH 11.0 with increasing pH. This trend indicates a decrease in H_3O^+ concentration accompanying the increase in OH^- at the microbubble interface. The diminished presence of H_3O^+ weakened the stability of the interfacial $SO_4^{\bullet-}$, while the excessive OH^- at the microbubble interface further scavenged the interfacial $SO_4^{\bullet-}$. Both of these factors collectively contributed to the suppressed oxidation performance under basic conditions.

The bubble size can affect the mass transfer of toluene as well as the enrichment of interfacial $SO_4^{\bullet-}$, and thus influencing the oxidation efficiency. In the sole microbubble system, the mass-transfer coefficients (K_{la}) of toluene increased from 0.0014 s^{-1} to 0.0087 s^{-1} when the bubble size reduced from 1500 μm to 350 μm (Supplementary Fig. 16), proving that smaller bubble sizes enhance toluene mass transfer. Additionally, K_{la} was markedly improved in the Co@SCN-PMS-microbubble system compared to the solo microbubble system. The enhancement of K_{la} should be attributed to the effective oxidation of toluene by interfacial $SO_4^{\bullet-}$. Importantly, this effect was more pronounced for smaller bubble sizes. For example, at a bubble size of 300 μm, the K_{la} increased markedly from 0.0087 s^{-1} (solo microbubble) to 0.0635 s^{-1} (Co@SCN-PMS-microbubble). In contrast, the enhancement of K_{la} was less prominent for the larger bubble size of 1500 μm, with K_{la} increasing from 0.0014 s^{-1} to 0.0069 s^{-1}. This phenomenon can be attributed to the larger specific surface area provided by smaller bubbles, facilitating the enrichment of both interfacial $SO_4^{\bullet-}$ and toluene at the interface, thereby enhancing the oxidation efficiency.

The stability of the Co@SCN-PMS-microbubble system was assessed through multiple additions of PMS. As depicted in Fig. 6c, the system exhibited long-term stability, maintaining a toluene removal efficiency of 99% over 600 min. Moreover, significant CO_2 production was observed during the process, suggesting complete oxidation of the toluene molecules. To further elucidate the remarkable stability, we employed ESR technology to monitor $SO_4^{\bullet-}$ generation during this extended period (Supplementary Fig. 17 and Supplementary Note 3). Our findings indicate that the intensity of $SO_4^{\bullet-}$ remained relatively constant, showing no significant decay throughout this period. This result strongly supports that $SO_4^{\bullet-}$ generated at the microbubble surface is stable, thereby ensuring their sustained efficacy in the oxidation of toluene. In addition to toluene, interfacial $SO_4^{\bullet-}$ was demonstrated highly effective removal (>97%) of various VOC pollutants in the Co@SCN-PMS-microbubble system, including ethyl acetate, chlorobenzene, benzene, and styrene, highlighting the broad applicability of interfacial $SO_4^{\bullet-}$ in VOCs treatment (Supplementary Fig. 18).

Furthermore, density functional theory (DFT) calculation was employed to understand the high oxidation capability of interfacial $SO_4^{\bullet-}$. The oxidation of toluene by $SO_4^{\bullet-}$ was selected as a model reaction to investigate the activation barriers in different phases. Recent work has revealed that the electron transfer at the methyl group (-CH_3) is the initial step for toluene oxidation on the water surface, yielding the benzyl radical[40]. Our product experiments further confirmed this oxidation pathway triggered by $SO_4^{\bullet-}$ in the Co@SCN-PMS-Microbubble system (Supplementary Figs. 19, 20, and Supplementary Note 4). Therefore, we compared the activation barriers for the $SO_4^{\bullet-}$-mediated electron-transfer reaction in different phases. As illustrated in Fig. 6d, the activation barriers were calculated to be 0.46 eV, 0.29 eV, and 0.22 eV in the gas phase, liquid phase, and at the interface, respectively. Importantly, the reaction at the interface had the lowest activation barrier, proving that $SO_4^{\bullet-}$ was most favorable for toluene oxidation at the interface rather than in the gas phase and liquid phase. Moreover, AIMD simulation provides another perspective of ultrafast oxidation of toluene by interfacial $SO_4^{\bullet-}$. As depicted in Supplementary Figs. 21 and 22, toluene molecules also exhibited minimum free energy at the gas-liquid interface, indicating that not only $SO_4^{\bullet-}$ but also toluene has the tendency to accumulate at the air–water interface. This behavior led to a significant increase in the concentrations of both $SO_4^{\bullet-}$ and toluene in the local microenvironment, thus facilitating their interactions and promoting the oxidation reactions (Fig. 6e).

We further calculated the reaction rate constants of $SO_4^{\bullet-}$ toward toluene in the interface and the bulk phase, respectively. Notably, the reaction rate constant of interfacial $SO_4^{\bullet-}$ toward toluene (k_{in}) was calculated to be 8.59×10^{10} M^{-1} s^{-1}, which surpassed that in the liquid phase by two orders of magnitude (7.78×10^8 M^{-1} s^{-1}) and that in the gas phase by four orders of magnitude (2.37×10^6 M^{-1} s^{-1}). Based on the reaction kinetics (detail shown in Supplementary Note 5), we further derived the decomposition rate of toluene (De) by interfacial $SO_4^{\bullet-}$ at a specific time (t), which was related to k_{in} and concentration of interfacial $SO_4^{\bullet-}$ ($[SO_4^{\bullet-}]_{in}$), as follows:

$$De = \left(1 - e^{-k_{in}[SO_4^{\bullet-}]_{in}t}\right) \times 100\% \quad (1)$$

The result shows that, within just 2 s, the interfacial $SO_4^{\bullet-}$ can achieve a remarkable decomposition rate of 99.0% for toluene. In contrast, the bulk $SO_4^{\bullet-}$ required 42.3 min to decompose 99.0% of toluene. Thus, the required time for complete toluene removal by interfacial $SO_4^{\bullet-}$ was shorter than the retention time of the toluene microbubble (7 s), while the time for bulk $SO_4^{\bullet-}$ was much longer. These findings confirm the complete oxidation of toluene within the microbubble by the interfacial $SO_4^{\bullet-}$, demonstrating the ultrafast oxidation capacity of the interfacial $SO_4^{\bullet-}$.

Discussion

The air–water interface of microbubbles represents an intriguing microenvironment with significant potential to accelerate ROS-induced reactions. However, the dynamic nature of microbubbles presents a challenge in probing ROS chemistry at this critical interface, leading to an underappreciation of their potential applications. We develop a catalyst-based strategy to investigate the interfacial ROS chemistry and explore its promising application, through the employment of an amphiphilic Co@SCN catalyst to trigger a Fenton-like reaction (Co@SCN-PMS) at the microbubble surface. The Co@SCN catalyst can stably attach to the microbubble interface, serving as a suitable medium to deliver the oxidant PMS from the bulk solution to the air–water boundary. This, in turn, triggers a fast Fenton-like reaction to produce a high concentration of $SO_4^{\bullet-}$ (~10^{-11} M) at the microbubble surface. We attribute the enhanced reactivity to the strong intrinsic electric field at the microbubble interface, which expedites the one-electron transfer between the single Co sites and PMS. This approach leverages the advantages of the air–water interface and helps us to understand the underlying mechanism.

Upon this approach, we reveal two important characteristics of interfacial $SO_4^{\bullet-}$. Firstly, our results demonstrate that the generated $SO_4^{\bullet-}$ preferentially reside at the air–water interface rather than in the bulk phase. We attribute this to the presence of the lowest free energy

of $SO_4^{\bullet-}$ at the air–water interface and the formation of strong hydrogen bonding interaction between $SO_4^{\bullet-}$ and H_3O^+ which provides a compelling stabilizing force $SO_4^{\bullet-}$ to localize at the interfacial region. Secondly, the interfacial $SO_4^{\bullet-}$ exhibits the lowest energy barrier and the highest oxidation reactivity toward VOCs pollutants like toluene with a rate constant of $10^{10}\,M^{-1}\,s^{-1}$, much higher than those in the bulk reactions by more than 2 orders of magnitude. These findings highlight the benefits of harnessing the air–water interface for accelerated ROS-induced reactions, offering a more comprehensive understanding of the interfacial ROS and its potential applications.

Overall, this study holds profound implications, as the micro-environment of the air–water interface and the high reactivity of ROS generated in this interface can drive advances across diverse fields, including environmental remediation, catalysis, biology, and organic synthesis. Particularly for environmental remediation, our findings open up new opportunities for advancing treatment technologies. For example, exploring innovative strategies to modulate the air–water interface could significantly enhance the efficient interaction between recalcitrant pollutants and the generated interfacial ROS. This extends not only to gaseous contaminants but also to hydrophobic aqueous pollutants. Furthermore, gaining a comprehensive understanding of the degradation pathways and transformation kinetics of pollutants at the air–water interface is essential to fully harness this crucial interface.

Methods

Characterization

The SEM image was taken using Zeiss GeminiSEM 300 (Carl Zeiss, Oberkochen, Germany) equipped with EDX unit (QUANTAX Bruker AXS Microanalysis) operated at an acceleration voltage of 4 kV and a working distance of 7 mm. The nanoscale structures were observed using HRTEM (JEOL JEM-2100F) with an accelerating voltage of 200 kV. Atomic-level high-angle annular dark-field scanning transmission electron microscopy (HAADF-STEM) images and the corresponding STEM-EDS elemental mapping profiles were taken on a JEOL JEM-ARM200F equipped with a CEOS probe corrector, with a guaranteed resolution of 0.08 nm. XAFS data were obtained by means of Athena and Artemis software according to standard procedures. The cobalt content in Co@SCN was analyzed by inductively coupled plasma atomic emission spectroscopy (ICP-OES). The FTIR spectra were recorded via a Nicolet 8700 FTIR spectrophotometer (Thermo Fisher Scientific Inc.). XAFS measurements at the Co K-edge were conducted at the BL14W1 beamline of the Shanghai Synchrotron Radiation Facility (SSRF). The Co@SCN sample was analyzed using fluorescence mode, while standard Co foil, CoO, and Co_3O_4 samples were analyzed using transmission mode. The acquired spectra were calibrated and processed using the Athena program within the IFEFFIT software package (version: 1.2.11d). Fourier transform (FT) of the Co K-edge EXAFS spectra in both k-space and R-space was performed with a k-weighting number of 3 and appropriate widths of Hanning window functions. Subsequently, these spectra were fitted based on the FEFF theory under the first-shell approximation using Co–O, Co–Co, and Co–N scattering paths in the Artemis software (version: 0.9.26).

Fluorescence imaging

Confocal fluorescence imaging was conducted using an inverted Zeiss LSM 780 AxioObserver laser scanning confocal microscope equipped with a 40×oil-type objective lens (EC Plan-Neofluar 40×/1.30 Oil DIC M27). A microbubble was introduced into the mixed solution containing Co@SCN/PMS/coumarin in rectangular glassware (dimensions: length × widt'h × height = 5 × 5 × 0.1 cm). To prevent the rapid bursting of the microbubble, an optically smooth glass plate was placed on top of the glassware. Imaging was performed within several seconds after introducing the microbubble into the mixed solution. Coumarin was selected as a representative probe for ROS, its oxidative product (7-hydroxycoumarin) can excite the specific fluorescence at 445 nm. All images were digitized and analyzed by ZEN imaging software.

Experimental Procedures

A photograph of the microbubble reactor is shown in Supplementary Fig. 23. A VOC gas with a certain concentration of 30 ppmv is achieved by mixing VOC vapor with a specific proportion of air, and the inlet flow rate is controlled at 200 mL min^{-1}. The VOC-microbubbles are generated by introducing the VOC gas into a bubble aerator, with the microbubble size controlled by varying the pore-size distribution of the bubble aerators. The reaction occurred as the microbubbles passed from the bottom of the microbubble reactor into the bulk of the mixed solution containing Co@SCN-PMS. The retention time (t_B) of microbubble within the solution bulk is about 7.0 s ($t_B = h/\upsilon_B$, where h is the height of solution bulk, υ_B is the velocity of bubble rise; for bubble diameters of 350 μm, the corresponding velocities are about 0.028 m s^{-1} from the high-speed video). The concentration of VOCs at both the inlet and outlet of the microbubble reactor was measured using a gas chromatograph (GC) equipped with flame-ionization detectors (FID) and a Rt-Q-BOND PLOT column (30 m × 0.25 mm id, film thickness 10 μm). The removal efficiency of VOCs in the gaseous phase was calculated from the following equation:

$$\text{Removal efficiency} = \frac{[\text{VOCs}]_{\text{inlet}} - [\text{VOCs}]_{\text{outlet}}}{[\text{VOCs}]_{\text{inlet}}} \times 100\% \quad (2)$$

where $[\text{VOCs}]_{\text{inlet}}$ and $[\text{VOCs}]_{\text{outlet}}$ are VOCs concentrations at the inlet and the outlet of the reactor, respectively.

Computational details

In this study, a combination of classic molecular dynamics (MD) and ab initio molecular dynamics (AIMD) simulations was employed to investigate the free energy variation and interfacial physical-chemical interactions between $SO_4^{\bullet-}$ (or toluene) and the water-gas interface. Initially, classical MD simulations were used to equilibrate the water solution for 300 ps (Supplementary Data 1). Following this equilibration, we constructed the simulation model by replacing several water molecules with the $SO_4^{\bullet-}$ or toluene molecule, which was then relaxed to a local minimum configuration (Supplementary Data 2, 3). This preparation was essential for the subsequent AIMD and metadynamics simulations aimed at determining the free energy profile and characterizing the transition states.

In the MD simulation, one oxygen (O) atom of the H_2O molecule in the solution was fixed, and the distance between this O atom and the $SO_4^{\bullet-}$ or toluene molecule was employed as a collective variable to reduce the dimension of reaction space for free energy calculation. The classic MD simulation was conducted using GROMACS 5.0, while AIMD simulations were performed using the CP2K-9.1 package. The configurations of $SO_4^{\bullet-}$ and toluene molecules in water, vacuum, and at the interface are presented in Supplementary Data 2 and 3, respectively. The generalized-gradient approximation with the parameterization of Perdew, Burke, and Ernzerhof (PBE) was utilized to compute the exchange-correlation energy. Given the significant hydrogen bonding interaction in the solution, the dispersion correction was accounted for using the empirical parameterized Grimme (D3) method.

Valence-shell electrons (1s1 for H, $2s^22p^2$ for C, $2s^22p^4$ for O, $3s^22p^4$ for S) were described using hybrid Gaussian and plane-wave (GPW) basis sets, with a cutoff energy of 600 Rydberg for auxiliary plane-wave basis sets during simulation and geometric relaxation. Brillouin zone integration was carried out with a reciprocal space mesh consisting only of the gamma point. Special triple-ζ valence plus polarization (TZVP) basis sets were employed to minimize basis set superposition errors, while core electrons were described with scalar relativistic norm-conserving pseudopotentials.

For free energy calculation, well-tempered single walker metadynamics simulations were conducted for up to 15 ps. The Nose-Hoover thermostat (NVT) was utilized in the simulations, with a time step of 1.0 fs and a total simulation run time of up to 9 ps to equilibrate the system at the density functional theory (DFT) level. Statistical sampling was performed at an elevated temperature of 298 K. To accurately calculate the transition states of $SO_4^{\bullet-}$ and evaluate the rate constants associated with the transition state energy barrier, we utilized the climbing image nudged-elastic-band (CI-NEB) method, applying a convergence criterion of 0.05 eV $Å^{-1}$.

Calculation of reaction rate constant

The reaction rate constant of $SO_4^{\bullet-}$ toward toluene in the interface and the bulk phase was calculated using the following transition state theory-based equation:

$$k = \frac{k_b T}{h}\left(\frac{RT}{P}\right)e^{-\Delta G/Tk_b} \quad (3)$$

Where k is the rate constant, k_b is Boltzmann's constant, T is temperature, h is the Planck constant, the RT/P is the inverse of the molar concentration, ΔG is the activation free energy of $SO_4^{\bullet-}$ with toluene in the interface or the bulk.

Reporting summary

Further information on research design is available in the Nature Portfolio Reporting Summary linked to this article.

Data availability

The data supporting the findings of the study are included in the main text and supplementary information files. All data of this study are available from the corresponding authors upon request. Source Data file has been deposited in Figshare under accession code DOI link https://doi.org/10.6084/m9.figshare.27055462. Source data are provided with this paper.

References

1. Ruiz-Lopez, M. F. et al. Molecular reactions at aqueous interfaces. *Nat. Rev. Chem.* **4**, 459–475 (2020).
2. Zhang, D. et al. High electric field on water microdroplets catalyzes spontaneous and ultrafast oxidative C–H/N–H cross-coupling. *J. Am. Chem. Soc.* **144**, 16184–16190 (2022).
3. Jordan, C. J. C. et al. Photooxidation of the phenolate anion is accelerated at the water/air interface. *J. Am. Chem. Soc.* **144**, 14012–14015 (2022).
4. Chen, H. et al. Spontaneous reduction by one electron on water microdroplets facilitates direct carboxylation with CO_2. *J. Am. Chem. Soc.* **145**, 2647–2652 (2023).
5. Liu, T. et al. Oxidation of sulfur dioxide by nitrogen dioxide accelerated at the interface of deliquesced aerosol particles. *Nat. Chem.* **13**, 1173–1177 (2021).
6. Wan, Z. et al. Mechanistic insights into the reactive uptake of chlorine nitrate at the air–water interface. *J. Am. Chem. Soc.* **145**, 944–952 (2023).
7. Rossignol, S. et al. Atmospheric photochemistry at a fatty acid–coated air-water interface. *Science* **353**, 699–702 (2016).
8. Xia, D. et al. Counterintuitive oxidation of alcohols at air–water interfaces. *J. Am. Chem. Soc.* **145**, 4791–4799 (2023).
9. Liang, Q. et al. Water charge transfer accelerates criegee intermediate reaction with H_2O^- radical anion at the aqueous interface. *J. Am. Chem. Soc.* **145**, 10159–10166 (2023).
10. George, C. et al. Heterogeneous photochemistry in the atmosphere. *Chem. Rev.* **115**, 4218–4258 (2015).
11. Liu, W. et al. Efficient hydrogen production from wastewater remediation by piezoelectricity coupling advanced oxidation processes. *Proc. Natl Acad. Sci. USA* **120**, e2218813120 (2023).
12. Liu, H.-Z. et al. Tailoring d-band center of high-valent metal-oxo species for pollutant removal via complete polymerization. *Nat. Commun.* **15**, 2327 (2024).
13. Wang, L. et al. A polymer tethering strategy to achieve high metal loading on catalysts for Fenton reactions. *Nat. Commun.* **14**, 7841 (2023).
14. Wu, J. H. et al. Unveiling singlet oxygen spin trapping in catalytic oxidation processes using in situ kinetic EPR analysis. *Proc. Natl Acad. Sci. USA* **120**, e2305706120 (2023).
15. Liang, Z. et al. Effective green treatment of sewage sludge from Fenton reactions: utilizing MoS_2 for sustainable resource recovery. *Proc. Natl Acad. Sci. USA* **121**, e2317394121 (2024).
16. Lee, J. et al. Persulfate-based advanced oxidation: critical assessment of opportunities and roadblocks. *Environ. Sci. Technol.* **54**, 3064–3081 (2020).
17. Yang, M. et al. Unveiling the origins of selective oxidation in single-atom catalysis via Co–N_4–C intensified radical and nonradical pathways. *Environ. Sci. Technol.* **56**, 11635–11645 (2022).
18. Zhao, Z. et al. Improved electronic structure from spin-state reconstruction of a heteronuclear Fe–Co diatomic pair to boost the Fenton-like reaction. *Environ. Sci. Technol.* **57**, 4556–4567 (2023).
19. Zhang, S. et al. Mechanism of heterogeneous Fenton reaction kinetics enhancement under nanoscale spatial confinement. *Environ. Sci. Technol.* **54**, 10868–10875 (2020).
20. Liu, T. et al. Water decontamination via nonradical process by nanoconfined Fenton-like catalysts. *Nat. Commun.* **14**, 2881 (2023).
21. Zhang, Y.-J. et al. Simultaneous nanocatalytic surface activation of pollutants and oxidants for highly efficient water decontamination. *Nat. Commun.* **13**, 3005 (2022).
22. Qiu, S. et al. A microbubble-assisted rotary tubular titanium cathode for boosting Fenton's reagents in the electro-Fenton process. *J. Hazar. Mater.* **424**, 127403 (2022).
23. Wang, K. & Pera-Titus, M. Microstructured gas-liquid-(solid) interfaces: a platform for sustainable synthesis of commodity chemicals. *Sci. Adv.* **10**, eado5448 (2024).
24. Sekiguchi, K. et al. Degradation of VOC gases in liquid phase by photocatalysis at the bubble interface. *Appl. Catal. B* **97**, 190–197 (2010).
25. Takahashi, M. et al. Free-radical generation from bulk nanobubbles in aqueous electrolyte solutions: ESR spin-trap observation of microbubble-treated water. *Langmuir* **37**, 5005–5011 (2021).
26. Takahashi, M. et al. Free-radical generation from collapsing microbubbles in the absence of a dynamic stimulus. *J. Phys. Chem. B* **111**, 1343–1347 (2007).
27. Zhou, S. et al. Untapped potential: applying microbubble and nanobubble technology in water and wastewater treatment and ecological restoration. *ACS EST Eng.* **2**, 1558–1573 (2022).
28. Chen, Y. et al. Atomic Fe dispersed on N-doped carbon hollow nanospheres for high-efficiency electrocatalytic oxygen reduction. *Adv. Mater.* **31**, e1806312 (2019).
29. Ha, Y. et al. Atomically dispersed Co-pyridinic N-C for superior oxygen reduction reaction. *Adv. Energy Mater.* **10**, 2002592 (2020).
30. Zhang, Y. et al. Continuous air purification by aqueous interface filtration and absorption. *Nature* **610**, 74–80 (2022).
31. Dedovets, D. et al. Multiphase microreactors based on liquid–liquid and gas–liquid dispersions stabilized by colloidal catalytic particles. *Angew. Chem. Int. Ed.* **61**, e202107537 (2022).
32. Nguyen, A. V. New method and equations for determining attachment tenacity and particle size limit in flotation. *Inter. J. Miner. Proc.* **68**, 167–182 (2003).
33. Garcia, R. Interfacial liquid water on graphite, graphene, and 2D materials. *ACS Nano* **17**, 51–69 (2022).

34. Qi, X. et al. Amphiphilic graphene composites. *Angew. Chem. Int. Ed.* **49**, 9426–9429 (2010).
35. Czili, H. & Horváth, A. Applicability of coumarin for detecting and measuring hydroxyl radicals generated by photoexcitation of TiO_2 nanoparticles. *Appl. Catal. B* **81**, 295–302 (2008).
36. Abadie, T. et al. Oxygen transfer of microbubble clouds in aqueous solutions – application to wastewater. *Chem. Eng. Sci.* **257**, 117693 (2022).
37. Vogel, Y. B. et al. The corona of a surface bubble promotes electrochemical reactions. *Nat. Commun.* **11**, 6323 (2020).
38. Gong, K. et al. Imaging of pH distribution inside individual microdroplet by stimulated Raman microscopy. *Proc. Natl Acad. Sci. USA* **120**, e2219588120 (2023).
39. Qu, W. et al. Self-accelerating interfacial catalytic elimination of gaseous sulfur-containing volatile organic compounds as microbubbles in a facet-engineered three-dimensional BiOCl sponge Fenton-like Process. *Environ. Sci. Technol.* **56**, 11657–11669 (2022).
40. Lee, K. et al. Catalyst-free selective oxidation of C(sp(3))-H bonds in toluene on water. *Nat. Commun.* **15**, 6127 (2024).

Acknowledgements

This work was financially supported by the National Natural Science Foundation of China (22306206 (R.X.) and 52200028 (K.G.)), the China Postdoctoral Science Foundation (2023M743992 (R.X.)), and the Guangdong Basic and Applied Basic Research Foundation (2023A1515010888 (R.X.)). The authors thank Prof. Peng Wang for helpful suggestions.

Author contributions

R.X. and K.G. conceived the research idea and designed the experiments. R.X., H.H., and H.Z. performed all the experiments and analyzed all the data. Y.L. performed the theoretical calculations. Y.Z., D.L., and H.H. discussed the results and commented on the manuscript. R.X. and K.G. co-wrote and revised the paper.

Competing interests

The authors declare no competing interests.

Additional information

Supplementary information The online version contains supplementary material available at https://doi.org/10.1038/s41467-024-53289-z.

Correspondence and requests for materials should be addressed to Haibao Huang.

Peer review information *Nature Communications* thanks Won Yong Choi and the other, anonymous, reviewers for their contribution to the peer review of this work. A peer review file is available.